Intraband cascade electroluminescence with weakly n-doped HgTe colloidal quantum dots 🙂

Cite as: J. Chem. Phys. 161, 124703 (2024); doi: 10.1063/5.0225746 Submitted: 26 June 2024 • Accepted: 4 September 2024 • **Published Online: 24 September 2024**











Xingyu Shen, D Augustin Caillas, D and Philippe Guyot-Sionnest Do



AFFILIATIONS

James Franck Institute, The University of Chicago, 929 E. 57th Street, Chicago, Illinois 60637, USA

Note: This paper is part of the JCP Festschrift in Honor of Yuen-Ron Shen.

^{a)}Author to whom correspondence should be addressed: pgs@uchicago.edu

ABSTRACT

Room temperature 6 µm intraband cascade electroluminescence (EL) is demonstrated with lightly n-doped HgTe colloidal quantum dots of ~8 nm diameter deposited on interdigitated electrodes in a metal-insulator-metal device. With quantum dot films of ~150 nm thickness made by solid-state-ligand-exchange, the devices emit at 1600 cm^{-1} (6.25 μ m), with a spectral width of 200 cm^{-1} , determined by the overlap of the $1S_e-1P_e$ intraband transition of the quantum dots and the substrate photonic resonance. At the maximum current used of 20 mA, the bias was 30 V, the external quantum efficiency was 2.7%, and the power conversion efficiency was 0.025%. Adding gold nano-antennas between the electrodes broadened the emission and increased the quantum efficiency to 4.4% and the power efficiency to 0.036%. For these films, the doping was about 0.1 electron/dot, the electron mobility was 0.02 cm 2 V $^{-1}$ s $^{-1}$, and the maximum current density was 0.04 kA cm $^{-2}$. Higher mobility films made by solution ligand exchange show a 20-fold increase in current density and a 10-fold decrease in EL efficiencies. Electroluminescence with weak doping is interesting for eventually achieving electrically driven stimulated emission, and the requirements for population inversion and lasing are discussed.

Published under an exclusive license by AIP Publishing. https://doi.org/10.1063/5.0225746

I. INTRODUCTION

The intersection of optics with liquids, interfaces, and nanomaterials has been a rich field of research in chemical physics. It led to nonlinear interfacial spectroscopy, in particular of the important water surface, ^{1–3} to the realization of giant optical enhancement with nanoscale roughened metal surfaces,4 and to the broad emergence of colloidal nanoscience with plasmonic and quantum dot nanocrystals. Basic studies of the size quantization of the energy levels of small colloidal semiconductor nanocrystals had a particularly broad impact.⁵ With appropriate protection of the interface dangling atomic bonds to provide bright emission in the visible spectrum, the "colloidal quantum dot" (CQD) chromophores are commercially used as phosphors in displays, lighting, and bioimaging. Much research is also exploring their use for solution processable optoelectronic devices, including transistors, photon detectors, and emitters,6 while electrically driven gain and stimulated emission were recently achieved in the visible.7

CQDs are readily extended to the near-infrared and beyond, where they can be much more efficient emitters than organic dyes. Bypassing the need for very small gap bulk semiconductors for "interband" infrared transitions, one can use the "intraband" transitions between the quantum confined states within the valence or conduction band for broad mid-infrared coverage.8 This approach originates with the solid state epitaxial quantum wells and dots. With wells, the 1D confinement creates sub-bands within the bulk conduction or valence bands, such that the transitions within the bands are called intersubbands. With appropriate doping, the infrared intersubband or intraband transitions in epitaxial quantum wells or dots of wider gap III-V materials have had a huge technological impact by providing infrared lasers, detectors, and non-linear optical

In the past decade, mid-infrared photodetection has been demonstrated with the intraband transitions of n-doped CQDs of HgSe, ^{13,14} HgTe, ¹⁵ PbS, ¹⁶ and Ag₂Se. ^{17,18} The performances are still lower than those using the interband transition of HgTe CQDs at

similar wavelengths, possibly because the requirement of narrow size dispersion is more stringent than for interband photodetection.¹⁹ However, mid-infrared electroluminescence (EL) with the intraband transitions of HgSe CQDs has recently been found to be more efficient than with the interband transitions of HgTe CQDs. 20-22 In particular, it was found that electrons, accelerated by a bias across a film of quantum dots, easily excite intraband transitions multiple times, in a process reminiscent of the quantum cascade in infrared intersubband quantum well lasers. The simplicity of the devices, combined with already notable performance, gives hope that CQD intraband cascade emission could become a new technology.

The prior work on CQD cascade emission used HgSe/CdS core/shell CQDs emitting at 5 µm. HgTe has a similar zero-gap inverted band structure as HgSe, and it should be equally possible to make HgTe CQD intraband cascade LEDs. One significant difference is that the tellurium pushes the conduction band of HgTe to a higher energy than HgSe.²³ As a result, with a chosen intraband transition at 5 μ m, HgSe CQDs are rather highly n-doped (between 1 and 2 electrons per dot), while HgTe is rather undoped (less than 0.1 e/dot), noting that the doping can be adjusted to some degree by synthetic conditions and the handling of the films.

In this work, we studied the slightly n-doped HgTe CQDs chosen to have an intraband transition around 5–7 μ m. The films are deposited on metal-insulator-metal (MIM) planar interdigitated electrodes optimized for a particular emission wavelength in the normal direction. Antennae within the electrode gaps are added to boost the emission efficiency. Compared to the mobility of 10^{-3} cm² V⁻¹ s⁻¹ with HgSe/CdS, the electron mobility of HgTe core-only CQDs films can be increased by orders of magnitude using polar exchange film fabrication.²⁴ The possibility of higher injection currents then motivates a discussion of population inversion and electrically driven mid-infrared lasing.

II. EXPERIMENTAL SECTION

A. Synthesis of HgTe QDs

The HgTe quantum dots studied here are made following a reported procedure that facilitates n-doping,²⁵ and they are approximately spherical with a diameter of 7.8 nm. For a typical reaction, 27 mg HgCl₂ (0.1 mmol) and 4 ml oleylamine are added to a 20 ml glass vial. The solution is heated at 100 °C in a glovebox to dissolve the HgCl₂. 14 µl (0.05 mmol) bis(trimethylsilyl)telluride (TMSTe) is diluted in 0.5 ml toluene and rapidly injected into the solution. The reaction is then allowed to proceed for 3 min. 8 ml of tetrachloroethylene (TCE) is added to quench the reaction. The solution is taken out of the glovebox, precipitated with ethanol, and centrifuged. The precipitate is dissolved in 3 ml of hexane or chlorobenzene, and the final solution is stored in a freezer.

B. Film preparation

Before making films, the CQD solution is cleaned a second time. 150 µl of HgTe QDs solution is precipitated with 20 µl 0.1M (di-n-dodecyl)dimethylammonium bromide (DDAB) in isopropanol (IPA) solution and ethanol. The solution is centrifuged, and the precipitate is dissolved in 300 µl of chlorobenzene/butyl acetate 1/10 solution. 30 µl of that solution is dropcasted on the desired substrate at 40 °C. The solution is lightly swirled to keep covering the substrate surface before wicking. For solid state ligand exchange, the dry film is first immersed in 10 mM HgCl₂ in methanol solution, rinsed with IPA, and dried with nitrogen. The film is then crosslinked with 1,2-ethanedithiol (EdT)/IPA 1/20 solution, rinsed with IPA, and dried with nitrogen. The process is repeated until the desired film thickness.

C. Solution ligand exchange

To transfer the CQDs to a polar solution, 50 µl dimethylformamide (DMF) and 10 µl 2-mercaptoethanol are added to 150 µl stock HgTe QDs in hexane solution. The solution separates into two phases, and the QDs quickly transfer to the polar phase. The clear nonpolar phase is discarded, and the polar phase is washed by adding 0.5 ml hexane. The polar phase is then precipitated with toluene and centrifuged. The precipitate is dissolved in 50–200 µl of DMF, which is then used to make films by spin-coating on the desired substrate at 40 °C. The substrate is then transferred to a 65 °C hotplate. The film is immersed in 10 mM HgCl2 in methanol solution, rinsed with IPA, and dried with nitrogen. The film is then crosslinked with EdT/IPA 1/20 solution, rinsed with IPA, and dried with nitrogen. The process is repeated until the desired film thickness.

D. Substrate fabrication

The grating MIM substrates are prepared on 2-in. sapphire wafers. The back reflector is made of 5 nm titanium, 50 nm gold, and 5 nm titanium using e-beam evaporation. The area is defined by photolithography. The Si spacer of 630 nm is deposited on the whole wafer by High Density Plasma Chemical Vapor Deposition (HDPCVD). The top interdigitated electrodes are made of 5 nm titanium and 50 nm gold using e-beam evaporation, with the area defined by photolithography.

For photolithography, the wafer is placed in a vacuum bake oven at 110 °C and primed with hexamethyldisilazane (HMDS). ~1 µm AZ MiR 703 photoresist is spincoated on top and baked at 95 °C for 1 min. The pattern is exposed to a 375 nm laser at a 120 mJ cm⁻² dose using Heidelberg MLA150. The wafer is then baked at 115 °C for 1 min. The wafer is immersed in AZ300 MIF developer with agitation for 1 min and rinsed with water.

For the antenna MIM substrates, both the electrodes and nanoantennas are patterned using electron beam lithography. The wafer is spin-coated with a layer of AR-P 6200-09 at 4000 rpm for 45 s and then baked at 150 °C for 1 min. A conductive layer of AR-PC 5090.02 is then spin-coated on top of the first resist layer, followed by baking at 90 °C for 2 min. The resist is exposed to a dose of 450 μC/cm², with the e-beam current set to 10 nA. The wafer is then rinsed with water to remove the conductive top layer of AR-PC 5090.02. The resist is developed in amyl acetate for 1 min and rinsed in IPA. Both the electrodes and nano-antennas are made of 5 nm titanium and 50 nm gold and deposited using e-beam evaporation.

E. PL and EL measurements

For the measurement of the photoluminescence (PL), the samples are excited with an 808 nm laser diode modulated by a sine wave at 40 kHz. The signal is collimated by a gold-coated f/2 parabolic mirror. The signal is then sent through a home-made step-scan Michelson interferometer to a cooled HgCdTe detector.

A silicon window is placed in front of the detector to filter out the laser. The detector output is sent through a lock-in amplifier. The interferometer is controlled by a step motor and scanned to give $50~{\rm cm}^{-1}$ resolution spectra. The PL spectrometer spectral response is determined using a blackbody at a known temperature so that the PL spectra are in relative units of emitted photon flux per wavenumber.

The EL spectra are taken using the same set up. The silicon window before the detector is removed since there is no 808 nm excitation. The electric current is driven by a Keithley Model 6221 AC and DC Source using a sine wave AC modulated at 2 kHz. A trigger signal with twice the current frequency is used for phase locking to the infrared detector. The voltage on the sample is measured using an oscilloscope or multimeter.

F. EQE and radiance determination

An absolute PL quantum yield measurement is performed for a reference undoped HgSe/CdSe sample film that emits mostly in the short-wave infrared around 4500 cm⁻¹. The film is made on a reflective aluminum substrate. The absolute integrated external quantum efficiency (EQE) of the reference sample is measured by inserting it inside a Spectralon integrating sphere. The PL and 808 nm signals are measured with a PbSe detector, with or without a silicon window filter, and with and without the sample. The quantum efficiency of the PbSe detector is assumed to be the same at all energies, in the

short wave and at 808 nm. The reference sample is then used to provide a relative EQE of samples emitting in the mid-infrared using the PL spectrometer, assuming that they have the same Lambertian emission, by normalizing the photon flux emitted and the absorbed 808 nm laser power. The EL radiance is obtained using the same method, and the EL EQE uses the injected electron number instead of the absorbed photon number.

G. FET measurements

The field-effect transistor (FET) substrates are made using a doped silicon wafer with 300 nm thermal SiO_2 . Interdigitated electrodes are made with photolithography. For low mobility dots, 125 pairs of 1 mm length electrodes with a 2 μ m gap size are used. For high mobility dots, 20 pairs of 0.45 mm long electrodes with a 10 μ m gap size are used. 1 V source-drain voltage is applied using a 6487 picoammeter/voltage source. The source-drain current is sent through the model SR570 low-noise current preamplifier. The gate voltage is applied using analog output of NI USB-6211 and JFIE 1432 dual HV AMP.

III. RESULT AND DISCUSSION

A. Low mobility devices

For low mobility devices, the quantum dots are capped with long aliphatic ligands and dissolved in a chlorobenzene/butyl acetate solution. The films are then made on substrates by drop casting,

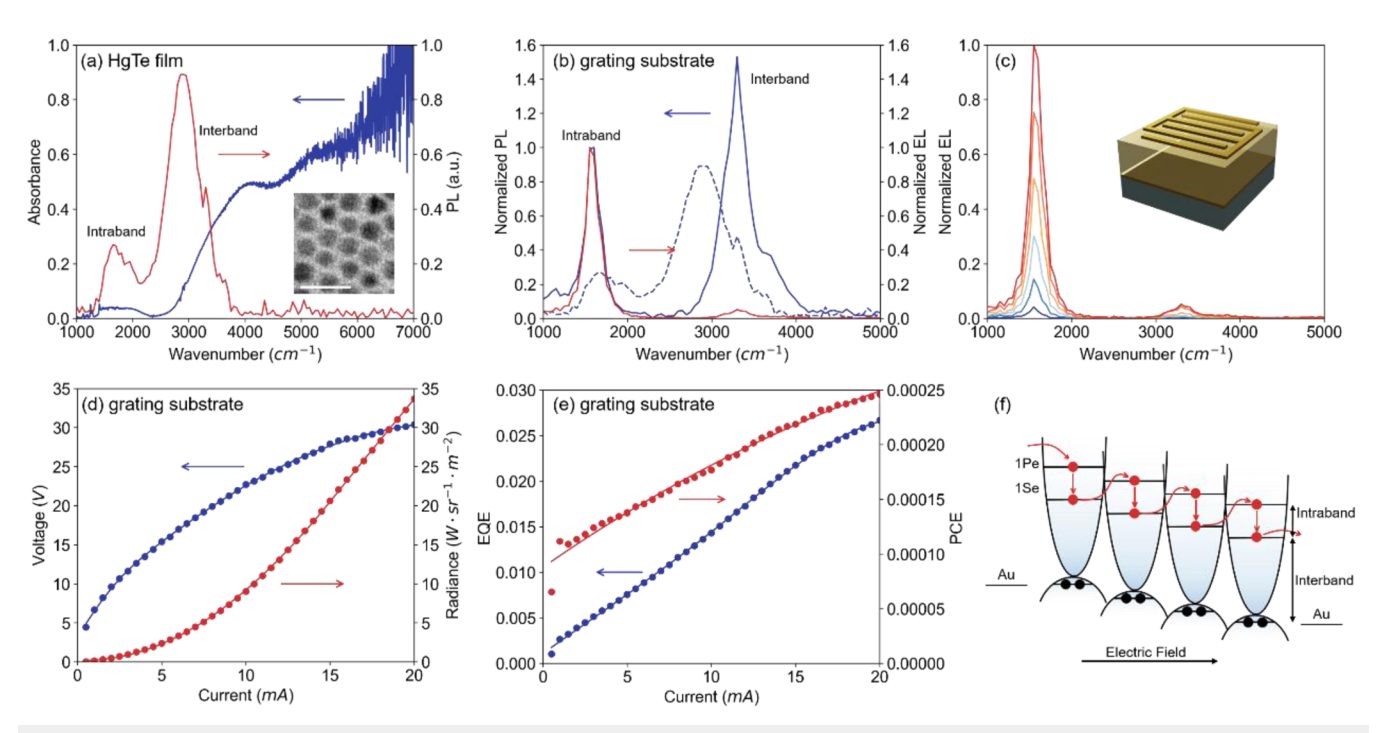


FIG. 1. (a) Absorption and PL spectra of HgTe dots film. The scale bar of the inset TEM picture is 20 nm. (b)–(e) EL properties measured on the grating substrate. (b) PL and EL spectra of HgTe dots on the grating substrate. The dotted line shows the PL of plain dots film for comparison. (c) EL spectra measured at different currents. (d) Current–Voltage–Radiance. (e) Current-EQE and PCE. (f) Figure 1(f). Energy level diagram. The $1S_e$ and $1S_h$ states are estimated to be 4.65 ± 0.1 and 5.05 ± 0.1 eV. The work function of gold is around 5.1 eV.

treated with a solution of HgCl₂, and crosslinked with ethanedithiol (EdT). The HgCl2 and EdT treatment follows prior work that showed a benefit for photodetection. ²⁶ Figure 1(a) shows the absorption and photoluminescence (PL) spectra of the films. The absorption is measured for a film on a ZnSe prism by attenuated total internal reflection. The interband edge rises between 2600 and 3600 cm⁻¹, with the "cutoff" defined as the half point on the edge, around 3100 cm⁻¹. A weaker intraband absorption, corresponding to the 1Se to 1Pe transitions, is present between 1500 and 2000 cm and indicates a weak doping of the 1S_e state. The PL is measured for a film deposited on an aluminum polished plate and is excited by an 808 nm pump laser. The interband PL in Fig. 1(a) is from 3500 to 2200 cm⁻¹, with a full width at half maximum (FWHM) of about 600 cm⁻¹ and a peak around 2800 cm⁻¹. The intraband PL is also broad, from 1400 to 2000 cm^{-1} (5–7 $\mu\text{m}) and overlaps with the tail$ of the interband PL.

For EL measurements, a thin film (150 nm) of dots is deposited on a grating metal–insulator–metal (MIM) substrate. The substrate comprises a back reflector, a 630 nm Si spacer, and top interdigitated electrodes with 0.6 μ m width and 2.4 μ m period. The spacer thickness and the electrode configuration are optimized through simulations to improve absorption for both intraband and interband, and this should also be optimal for emission. The simulated absorption spectrum is shown in Figs. 2(a) and S2(a), where absorption near 1600 and 3200 cm⁻¹ is largely improved and narrowed.

Figure 1(b) shows the measured PL and EL spectra. The PL spectrum shows both interband and intraband emission but is

narrowed by the photonic resonances, consistent with the simulations. The EL is obtained by driving a current between the electrodes using a symmetric sine wave AC modulated at 2 kHz. The EL is measured by the lock-in signal at 4 kHz. The spectrum is dominated by intraband emission, with a peak at 1600 cm $^{-1}$ (6.25 μm) and a FWHM of 200 cm $^{-1}$. Figure 1(c) shows that the intraband EL intensity increases with larger driving currents. Figure 1(d) shows the bias and EL radiance as a function of current. For a current of 20 mA, the voltage is 30 V, and the radiance reaches 34 W sr $^{-1}$ m $^{-2}$, assuming Lambertian emission. Figure 1(e) shows the electron to photon external quantum efficiency (EQE), which increases with the driving current, with a nearly linear dependence above 1 mA and reaching 2.7% at 20 mA. Figure 1(f) shows the power conversion efficiency (PCE), increasing from about 0.01% at low current to 0.025% at 20 mA.

B. Antenna enhancement

An antenna MIM is made by adding gold nano-crosses between the interdigitated electrodes. This design was recently used to enhance the photodetection performances and photoluminescence of HgTe CQDs in the mid-infrared. The antenna MIM has the same back reflector and 630 nm silicon spacer as the grating MIM, but the interdigitated electrodes are modified to fit the antennas. The electrodes have 2 μm width and 4 μm spacing, and the cross antennas have arms of 2 μm length and 0.2 μm width. Only one antenna fits within the electrode spacing while they repeat every 4 μm in the direction parallel to the electrodes.

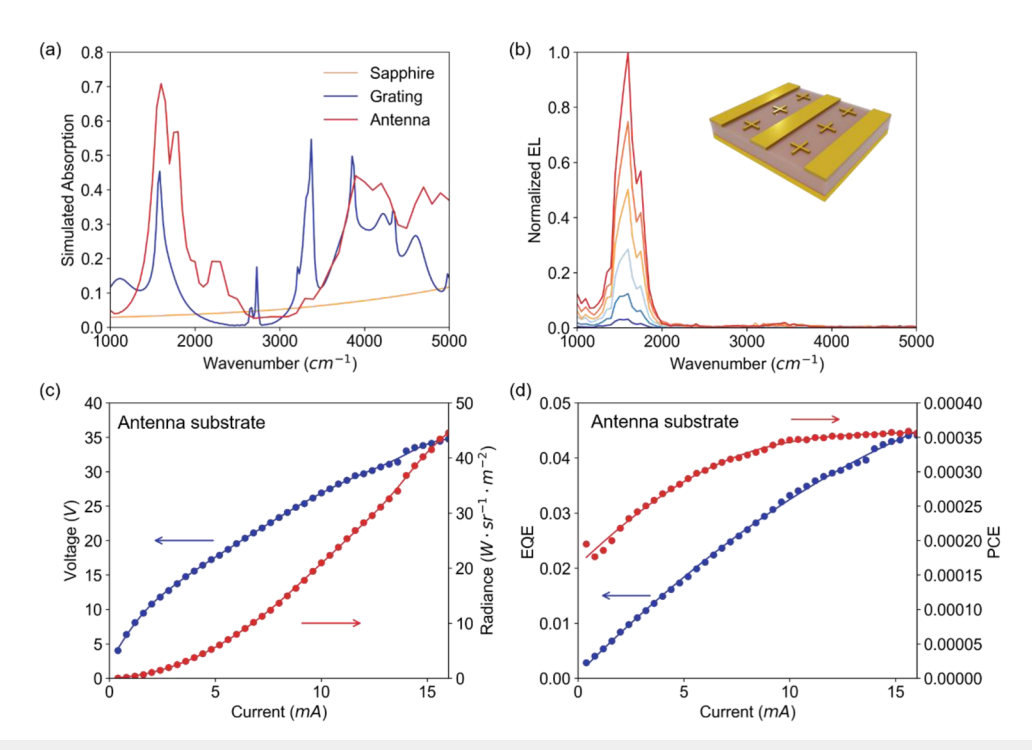


FIG. 2. (a) Simulated absorption of 200 nm CQD film on the antenna substrate, 150 nm CQD film on the grating substrate, and 150 nm CQD film on sapphire. (b)–(d) EL properties measured on the antenna substrate. (b) EL spectra measured at different currents. (c) Current–Voltage–Radiance. (d) Current-EQE and Current-PCE.

This structure is then covered with a 200 nm film of HgTe CQDs. Figure 2(a) shows that the simulated absorption around the intraband transition is broader and stronger for the 200 nm film on the antenna MIM, compared to the previous 150 nm film on the grating MIM. The dots films are modeled as a spectrally smooth absorber with an index of 2.3 + 0.1j. Figure 2(b) shows the EL spectra for the device made on the antenna MIM substrate, and it matches well the simulated spectrum in Fig. 2(a). Figure 2(c) shows the bias and EL intensity as a function of drive current. Compared to the grating MIM device in Fig. 1(d), the antenna-MIM device has a slightly larger resistance consistent with the larger electrode spacing but otherwise similar behavior. With a current of 16 mA, the radiance is 45 W sr⁻¹ m⁻², EQE reaches 4.4%, and PCE reaches 0.036%. There is, therefore, a benefit of the antenna MIM over the grating MIM structure.

C. Doping effects with FET measurements

The effect of doping is studied by making a thinner 50 nm CQD film on a Si/SiO $_2$ FET substrate. Figure 3(a) shows the source drain modulation with the gate voltage. The minimum around -3 V is attributed to 0 electron/dot, while the maximum around 30 V is attributed to 1 electron/dot. The gate voltage associated with one electron per dot is, therefore, around 30 V, in fair agreement with the FET dielectric capacitance and dot–dot distance of 8 nm. The gate voltage minimum at -3 V indicates that the film is slightly n-doped, with around 0.1 electron/dot. The electron mobility is

 $0.02 \text{ cm}^2 \text{ V}^{-1} \text{ s}^{-1}$ and the hole mobility is $0.0015 \text{ cm}^2 \text{ V}^{-1} \text{ s}^{-1}$. Even with the low n-doping, the electrons still dominate the transport. The hole density can be estimated by considering that the intrinsic CQDs carried density is given by $n_i \sim \sqrt{N_c N_v} \exp$ $\left(-\frac{E_g}{2kT}\right)$ = 0.0015/dot, where it is assumed that $N_c = N_v = 2$ for the conduction and valence band density of states, $E_g = 0.37$ eV is the bandgap, and T = 300 K. With an electron density of n = 0.1/dot, the hole density is $p = n_i^2/n = 0.00002/dot$, which confirms that electrons dominate the transport. Figure 3(b) shows that the drainsource bias decreases with increasing positive gate bias and this is consistent with the gate increasing the electron density. Figure 3(c) shows that the EL signal is about constant with the positive gate bias, and decreases with a negative gate bias. Figure 3(d) summarizes these effects by showing the power efficiency as a function of gate voltage. This indicates that further n-doping increases the EL efficiency slightly, and p-doping decreases EL emission.

Thus, while intraband detectors require the precise electron filling of the lowest electronic state, this work shows that intraband EL works with slight n-doping. Prior work on HgSe/CdS cascade EL at 5 μm showed higher efficiencies, and the optimum doping was around 0.5 electrons per dot. Slight n-doping may be beneficial because it ensures that holes are minority carriers, and this should help the intraband emission by eliminating hole-Auger relaxation. Slight n-doping also fills all electron traps. In future work, trap free and intrinsically wider gap dots with only electron injection layers might be candidates for cascade intraband emission, which could broaden the range of materials possible.

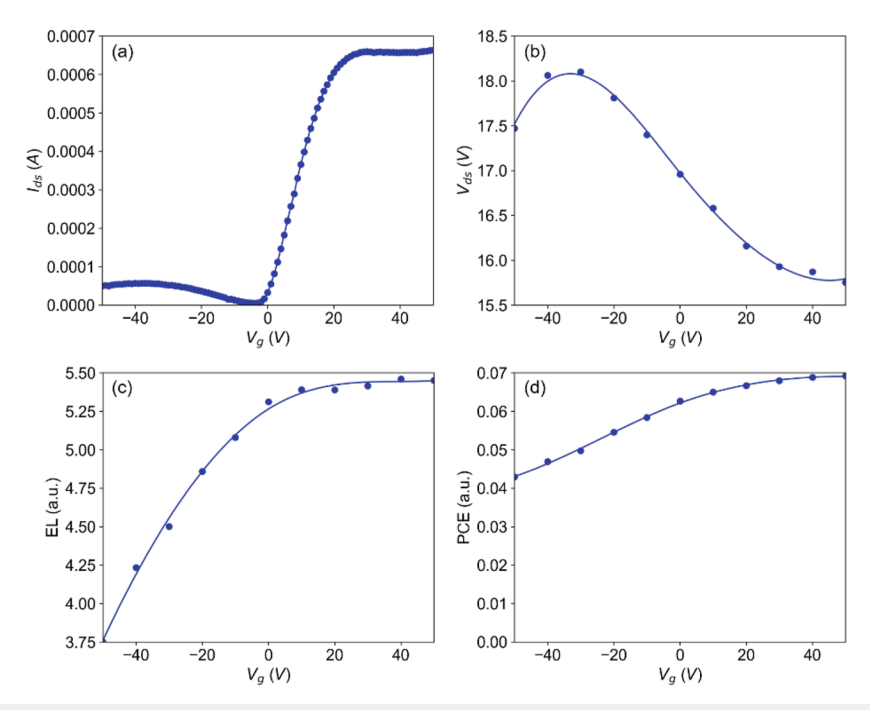


FIG. 3. Measurements with the bottom gate electrode at 300 K. (a) The device is driven by a constant drain source voltage, and the drain source is measured with different gate biases. (b)–(d) The device is driven by a constant AC. The drain source voltage (b) and EL signal (c) are monitored at different gate biases. The relative power efficiency (d) is calculated from EL/V_{ds}.

D. High mobility devices using solution ligand exchange

Advances in ligand exchange strategies have led to higher mobility quantum dot films, with several reports of improved optical performances. 29-31 High mobility readily allows higher current density, and this might translate to brighter EL. Solution ligand exchange of the HgTe dots is done by transfer to a polar DMF solvent. This removes the long chain ligands, which leads to closer dot-to-dot packing in films and increases mobility. The CQD polar ink is spin-coated to form thin films and dried at 65 °C. The film is then treated with HgCl₂ and EdT so that the dots are slightly n-doped, with about 0.1 electron/dot. 24.29 Figure 4(a) shows the source-drain current as a function of gate voltage on a regular FET. Compared to the low-mobility CQD preparation used above, the solution ligand exchange mobilities are about 100× larger, reaching 1.6 cm² V⁻¹ s⁻¹ for electrons and 0.2 cm² V⁻¹ s⁻¹ for holes, comparable to prior reports for this HgTe dot size. 29

For EL measurements, the dots are spin-coated on the grating MIM substrate to form very thin films (~10 nm). The need for the very thin film is due to the maximum current possible with the current source used for testing. Figure 4(b) shows measurable EL spectra from such a 10 nm film, with a clear intraband emission and a much weaker interband emission. The intraband emission is still around 1600 cm⁻¹ but it is accompanied by some emission on the red side and a small interband peak at 3200 cm⁻¹. The long

wavelength emission increases more than the 1600 cm⁻¹ emission with current. The possibility of thermal emission was therefore tested by changing the phase of the lock-in amplifier, and this shows that thermal emission is less than 10% of the emission peak (SI). The tail emission around 10 μ m is, therefore, not entirely thermal, but its origin is still unclear, possibly related to emission from higher energy levels. Figure 4(c) shows the AC voltage and EL radiance as functions of AC. Figure 4(d) shows the EQE and PCE as a function of the AC. Qualitatively, the EQE increase with increasing current is similar for these very thin high mobility films and the thicker low mobility films. However, the PCE decrease with increasing current is different and possibly related to the higher heat generated per volume. With 30 mA current, the voltage is 37 V, EQE is 0.38%, and PCE is 0.0029%. Thus, the EQE and PCE are about $10\times$ smaller with the high mobility films. With a 30 mA driving current, the device shows reversible EL properties at this large current density, but degradation is observed above 80 mA, leading to an irreversible redshift of the emission peak, which is then clearly a thermal contribution.

E. Possibility of electrically driven population inversion and lasing

The device above includes 166 pairs of electrodes with a period of 3 μ m, which covers a 1 mm² area. With a 10 nm dots film, the device area is 3.3×10^{-5} cm², and the 30 mA current corresponds

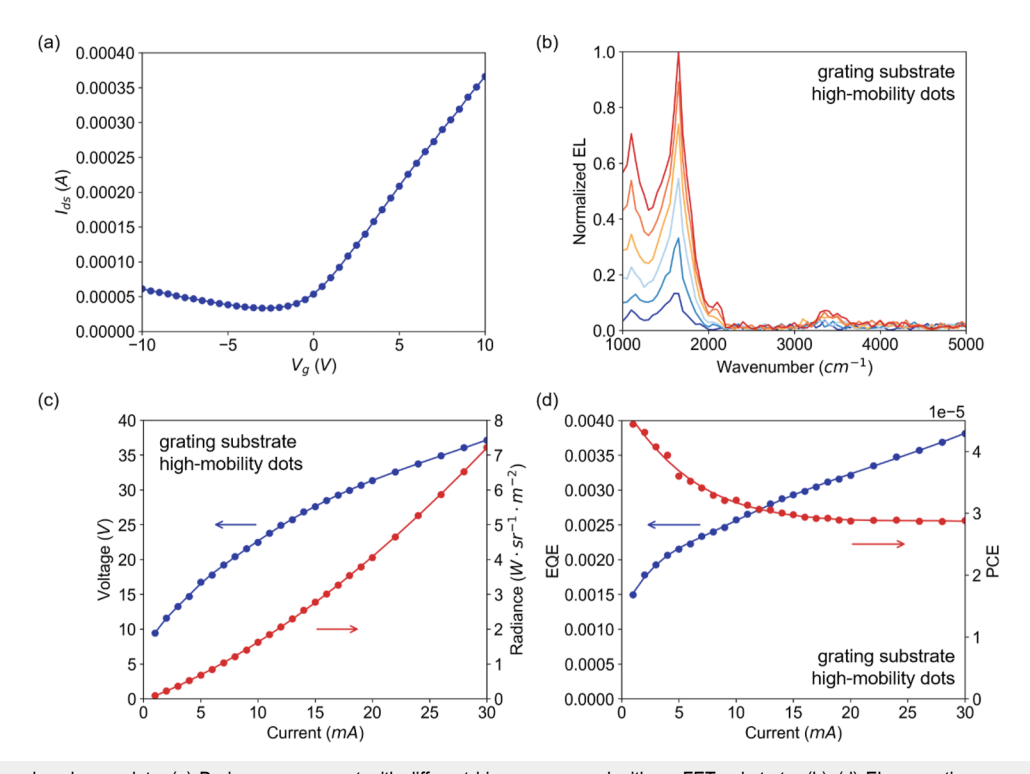


FIG. 4. Solution ligand exchange dots. (a) Drain-source current with different biases measured with an FET substrate. (b)–(d) EL properties measured with the grating substrate. (b) EL spectra at different currents. (c) Current–Voltage–Radiance. (d) EQE and PCE. For reproducibility, the PCE of four different devices around 22 V is $(3.2 \pm 0.3) \times 10^{-5}$.

to a current density of about 0.9 kA/cm². Thus, despite the lower EL efficiencies, the large current density merits discussion in the context of electrically driven CQD lasers. In the visible and near IR, achieving stimulated emission in interband CQDs is difficult due to the degeneracy of band edge states, which requires multiple excitons per dot for population inversion, and the resulting fast nonradiative Auger relaxation. Strategies explored to reduce the lasing threshold include suppressing Auger decay,³² n-doping the dots,^{33–35} and reducing the degeneracy of the band edge levels.³⁶ With intrinsic or slightly n-doped quantum dots, there is only a small absorption at the intraband emission wavelength, and reaching the gain threshold should be an easier target.

The first requirement for intraband lasing is an inversion of the $1S_e-1P_e$ population. Starting from a low doped system, this needs a faster electron injection from $1S_e$ to $1P_e$ than the $1P_e-1S_e$ relaxation. Figure 5 shows a simple rate equation model. For each dot, only $1S_e$ and $1P_e$ are considered. Process 2 is the $1P_e-1S_e$ relaxation in a dot. The relaxation time is taken to be $\tau_2=100$ ps, roughly consistent with the 10^{-3} PL quantum yield. Processes 3, 4, and 5 are the electron transfers from $1S_e$ to $1P_e$, from $1S_e$ to $1S_e$, and from $1P_e$ to $1P_e$ between adjacent dots. The electron transfer times are taken to be the drift time from dot to dot, which is estimated from the mobility and the bias across dots. With an electron mobility of $1.6 \text{ cm}^2 \text{ V}^{-1} \text{ s}^{-1}$, the drift time is about $\tau_3 \sim 3.3 \text{ ps}$ with a bias of 0.12 V (~mid gap) between neighboring dots. n_1 and n_2 are the electron densities in states 1 ($1S_e$) and 2 ($1P_e$), respectively, and they are considered uniform in the film.

The rate equations relating n_1 and n_2 are then

$$\frac{dn_1}{dt} = \frac{n_2(g_1 - n_1)}{\tau_2} - \frac{n_1(g_2 - n_2)}{\tau_3},$$

$$\frac{dn_2}{dt} = -\frac{n_2(g_1 - n_1)}{\tau_2} + \frac{n_1(g_2 - n_2)}{\tau_3},$$

where $g_1=2$ and $g_2=6$ are the degeneracy of states. In steady state, $\frac{dn_1}{dt}=\frac{dn_2}{dt}=0$. Since the doping is low, $n_1,\ n_2\ll g_1,\ g_2$, this simplifies to $\frac{n_2g_1}{\tau_2}=\frac{n_1g_2}{\tau_3}$. The electron density ratio of the two states is then $\frac{n_2}{n_1}=\frac{g_2\tau_2}{g_1\tau_3}=90$. This large population inversion benefits from the short drift time as well as the higher degeneracy of $1P_e$. The rate model also shows that population inversion should not appear in the low mobility case because $\tau_3>\tau_2$.

The rate equation also informs on the spontaneous emission power efficiency of the device, which is proportional to the ratio of

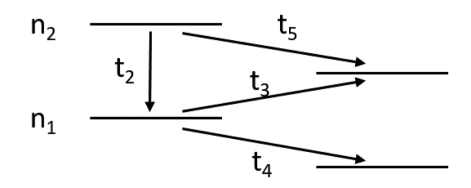


FIG. 5. Schematic of rate equation model. For the intraband transition of HgTe dots, state 1 is the $1S_e$ state, and state 2 is the $1P_e$ state.

the relaxation rate in the dot divided by the Ohmic loss, which is proportional to the total transfer between dots,

$$PCE \sim \frac{\frac{g_1 n_2}{\tau_2}}{\frac{g_2 n_1}{\tau_3} + \frac{g_1 n_1}{\tau_4} + \frac{g_2 n_2}{\tau_5}} = \frac{\frac{g_2 n_1}{\tau_3}}{\frac{g_2 n_1}{\tau_3} + \frac{g_1 n_1}{\tau_4} + \frac{g_2 n_2}{\tau_5}} = \frac{g_2}{g_2 + g_1 \frac{\tau_3}{\tau_4} + g_2 \frac{\tau_3}{\tau_5} \frac{n_2}{n_1}}.$$

This shows that the $1P_e$ to $1S_e$ relaxation affects the efficiency through the population ratio n_2/n_1 , while the transfer rate ratios τ_3/τ_4 and τ_3/τ_5 also affect the efficiency. The efficiency increases when the electron transport from $1S_e$ to $1P_e$ (τ_3) is faster than the transport between the same states (τ_4 , τ_5). This should arise at resonance when the bias per dot is close to the $1S_e-1P_e$ energy. The rate treatment shows that a large population inversion, n_2/n_1 , reduces the spontaneous emission power efficiency, even though it is needed for lasing. Thus, the high mobility suppresses spontaneous emission, and this is beneficial for stimulated emission.

Finally, the gain coefficient is calculated using $g=(n_2-n_1)\alpha_g$, where α_g is the gain coefficient. α_g is related to the absorption coefficient α_a by the state degeneracy. In spherical dots, the $1S_e-1P_e$ transitions are split by spin–orbit, leading to a lower energy $1S_e-1P_{e1/2}$ transition, and HgTe dots showed an imaginary refractive index k=0.6 at the peak of the $1S_e-1P_{e1/2}$ transition with the $1S_e$ filled with 2 electrons. This corresponds to an absorption coefficient $\alpha_a=4\pi k/\lambda=12\,000$ cm⁻¹. An even greater absorption coefficient is expected here given that the previous value was for longer wavelength transitions and lower dot packing densities. Nevertheless, considering that $1P_{e1/2}$ and $1S_e$ have the same degeneracy $g_1=g_2=2$, the emission coefficient is $\alpha_g=\alpha_a=6000$ cm⁻¹. Assuming a small 10% population inversion $(n_2-n_1)=0.1$, the gain could then be g>500 cm⁻¹.

This gain magnitude should be sufficient to counter losses with dedicated resonator structures. One inherent loss is absorption in the film of quantum dots itself. Using the energy transfer model previously introduced for explaining the low intraband PL quantum yield of $\sim\!10^{-3}$ – 10^{-4} , 37 we estimate that the matrix loss coefficient is less than about 100 cm $^{-1}$ and it should, therefore, be manageable. The MIM structures used here will likely be too lossy and will need to be replaced by dielectric structures. There will also be difficulties finding appropriate electrode materials compatible with the solution processing. However, the discussion above is a motivation to pursue the fabrication of optimized structures for lasing.

IV. CONCLUSION

In summary, this work demonstrates the use of the intraband transition of lightly doped HgTe CQDs for room temperature electrically driven spontaneous emission light sources around 6 μm . The work also discusses the possibility of electrically driven mid-infrared gain. The optimum doping is in the low n-type range, with the electron current dominating transport. Using different preparations, films of the same HgTe CQDs with 0.01 and 1 cm² V $^{-1}$ s $^{-1}$ electron mobility were tested. The higher mobility dots film preparation provides $10\times$ lower emission power efficiency but a much larger current density, around 1 kA cm $^{-2}$. A simple rate model shows that such current densities should give a high population inversion. From the absorption strength and fine structure of the intraband transition, a gain coefficient of $\sim\!500~\text{cm}^{-1}$ might be feasible even with a 10%

inversion. Optical resonator structures with low doping, high mobility dots will therefore be beneficial for electrically driven mid-infrared lasing with colloidal quantum dots.

SUPPLEMENTARY MATERIAL

The supplementary material encompasses grating substrate structure, antenna substrate simulation, thermal emission, matrix absorption coefficient, and gate leakage current of FET substrates.

ACKNOWLEDGMENTS

The work is supported by Grant Nos. NSF-ECCS-2226311 and ARO78821-EL. X.S. is supported by the Martha Ann and Joseph A. Chenicek Fellowship from the chemistry department. This work made use of the shared facilities at the University of Chicago Materials Research Science and Engineering Center, supported by the National Science Foundation under Award No. DMR-2011854, and the Pritzker Nanofabrication Facility, part of the Pritzker School of Molecular Engineering at the University of Chicago that receives the support from the Soft and Hybrid Nanotechnology Experimental (SHyNE) Resource (Grant No. NSF-ECCS-2025633), a node of the National Science Foundation's National Nanotechnology Coordinated Infrastructure. This work was completed in part with resources provided by the University of Chicago's Research Computing Center.

AUTHOR DECLARATIONS

Conflict of Interest

The authors have no conflicts to disclose.

Author Contributions

Xingyu Shen: Conceptualization (equal); Investigation (equal); Methodology (equal); Writing – original draft (equal); Writing – review & editing (equal). **Augustin Caillas**: Investigation (equal); Writing – review & editing (equal). **Philippe Guyot-Sionnest**: Conceptualization (equal); Funding acquisition (equal); Supervision (equal); Writing – original draft (equal); Writing – review & editing (equal).

DATA AVAILABILITY

The data that support the findings of this study are available from the corresponding author upon reasonable request.

REFERENCES

- ¹Y. R. Shen, "Surface properties probed by second-harmonic and sum-frequency generation," Nature 337(6207), 519–525 (1989).
- ²P. Guyot-Sionnest, J. H. Hunt, and Y. R. Shen, "Sum-frequency vibrational spectroscopy of a Langmuir film: Study of molecular orientation of a two-dimensional system," Phys. Rev. Lett. **59**(14), 1597 (1987).

- ³Q. Du, R. Superfine, E. Freysz, and Y. Shen, "Vibrational spectroscopy of water at the vapor/water interface," Phys. Rev. Lett. **70**(15), 2313 (1993).
- ⁴G. T. Boyd, T. Rasing, J. R. R. Leite, and Y. R. Shen, "Local-field enhancement on rough surfaces of metals, semimetals, and semiconductors with the use of optical second-harmonic generation," Phys. Rev. B **30**(2), 519 (1984).
- ⁵A. L. Efros and L. E. Brus, "Nanocrystal quantum dots: From discovery to modern development," ACS Nano 15(4), 6192–6210 (2021).
- ⁶F. P. García de Arquer, D. V. Talapin, V. I. Klimov, Y. Arakawa, M. Bayer, and E. H. Sargent, "Semiconductor quantum dots: Technological progress and future challenges," Science **373**(6555), eaaz8541 (2021).
- ⁷N. Ahn, C. Livache, V. Pinchetti, H. Jung, H. Jin, D. Hahm, Y.-S. Park, and V. I. Klimov, "Electrically driven amplified spontaneous emission from colloidal quantum dots," Nature **617**(7959), 79–85 (2023).
- ⁸P. Guyot-Sionnest and M. A. Hines, "Intraband transitions in semiconductor nanocrystals," Appl. Phys. Lett. **72**(6), 686–688 (1998).
- ⁹Y. Yao, A. J. Hoffman, and C. F. Gmachl, "Mid-infrared quantum cascade lasers," Nat. Photonics **6**(7), 432–439 (2012).
- ¹⁰ A. Krier, E. Repiso, F. Al-Saymari, P. Carrington, A. Marshall, L. Qi, S. Krier, K. Lulla, M. Steer, and C. MacGregor, "Mid-infrared light-emitting diodes," in *Mid-Infrared Optoelectronics* (Elsevier, 2020), pp. 59–90.
- ¹¹D. Jung, S. Bank, M. L. Lee, and D. Wasserman, "Next-generation mid-infrared sources," J. Opt. 19(12), 123001 (2017).
- ¹²D. Botez and M. A. Belkin, Mid-Infrared and Terahertz Quantum Cascade Lasers (Cambridge University Press, 2023).
- 13 Z. Deng, K. S. Jeong, and P. Guyot-Sionnest, "Colloidal quantum dots intraband photodetectors," ACS Nano $8(11),\,11707-11714$ (2014).
- ¹⁴C. Livache, B. Martinez, N. Goubet, C. Gréboval, J. Qu, A. Chu, S. Royer, S. Ithurria, M. G. Silly, B. Dubertret, and E. Lhuillier, "A colloidal quantum dot infrared photodetector and its use for intraband detection," Nat. Commun. **10**(1), 2125 (2019).
- 15 H. Zhang, J. C. Peterson, and P. Guyot-Sionnest, "Intraband transition of HgTe nanocrystals for long-wave infrared detection at 12 μ m," ACS Nano 17(8), 7530–7538 (2023).
- ¹⁶I. i. Ramiro, O. Özdemir, S. Christodoulou, S. Gupta, M. Dalmases, I. Torre, and G. Konstantatos, "Mid- and long-wave infrared optoelectronics via intraband transitions in PbS colloidal quantum dots," Nano Lett. 20(2), 1003–1008 (2020)
- ¹⁷S. B. Hafiz, M. M. Al Mahfuz, and D.-K. Ko, "Vertically stacked intraband quantum dot devices for mid-wavelength infrared photodetection," ACS Appl. Mater. Interfaces 13(1), 937–943 (2020).
- 18 M. Park, D. Choi, Y. Choi, H.-b. Shin, and K. S. Jeong, "Mid-infrared intraband transition of metal excess colloidal $\rm Ag_2Se$ nanocrystals," ACS Photonics 5(5), 1907–1911 (2018).
- ¹⁹M. Chen, G. Shen, and P. Guyot-Sionnest, "Size distribution effects on mobility and intraband gap of HgSe quantum dots," J. Phys. Chem. C 124(29), 16216–16221 (2020).
- ²⁰X. Shen, A. Kamath, and P. Guyot-Sionnest, "Mid-infrared cascade intraband electroluminescence with HgSe–CdSe core–shell colloidal quantum dots," Nat. Photonics 17(12), 1042–1046 (2023).
- 21 X. Shen, J. C. Peterson, and P. Guyot-Sionnest, "Mid-infrared HgTe colloidal quantum dot LEDs," ACS Nano 16(5), 7301–7308 (2022).
- ²²X. Shen and P. Guyot-Sionnest, "Mid-infrared intraband electroluminescence on planar interdigitated electrodes," Matter 7, 1750 (2024).
- ²³M. Chen and P. Guyot-Sionnest, "Reversible electrochemistry of mercury chalcogenide colloidal quantum dot films," ACS Nano 11(4), 4165–4173 (2017)
- ²⁴ X. Lan, M. Chen, M. H. Hudson, V. Kamysbayev, Y. Wang, P. Guyot-Sionnest, and D. V. Talapin, "Quantum dot solids showing state-resolved band-like transport," Nat. Mater. 19(3), 323–329 (2020).
- ²⁵G. Shen, M. Chen, and P. Guyot-Sionnest, "Synthesis of nonaggregating HgTe colloidal quantum dots and the emergence of air-stable n-doping," J. Phys. Chem. Lett. **8**(10), 2224–2228 (2017).

- ²⁶M. M. Ackerman, M. Chen, and P. Guyot-Sionnest, "HgTe colloidal quantum dot photodiodes for extended short-wave infrared detection," Appl. Phys. Lett. 116(8), 083502 (2020).
- ²⁷ A. Caillas and P. Guyot-Sionnest, "Uncooled high detectivity mid-infrared photoconductor using HgTe quantum dots and nanoantennas," ACS Nano 18, 8952 (2024).
- ²⁸ A. L. Efros, V. Kharchenko, and M. Rosen, "Breaking the phonon bottleneck in nanometer quantum dots: Role of Auger-like processes," Solid State Commun. 93(4), 281–284 (1995).
- ²⁹X. Xue, M. Chen, Y. Luo, T. Qin, X. Tang, and Q. Hao, "High-operating-temperature mid-infrared photodetectors via quantum dot gradient homojunction," Light: Sci. Appl. **12**(1), 2 (2023).
- ³⁰M. Chen, Q. Hao, Y. Luo, and X. Tang, "Mid-infrared intraband photodetector via high carrier mobility HgSe colloidal quantum dots," ACS Nano **16**(7), 11027–11035 (2022).
- ³¹ J. Yang, H. Hu, Y. Lv, M. Yuan, B. Wang, Z. He, S. Chen, Y. Wang, Z. Hu, M. Yu *et al.*, "Ligand-engineered HgTe colloidal quantum dot solids for infrared photodetectors," Nano Lett. 22(8), 3465–3472 (2022).

- ³²N. Ahn, C. Livache, V. Pinchetti, and V. I. Klimov, "Colloidal semiconductor nanocrystal lasers and laser diodes," Chem. Rev. 123(13), 8251–8296 (2023).
- ³³K. Wu, Y.-S. Park, J. Lim, and V. I. Klimov, "Towards zero-threshold optical gain using charged semiconductor quantum dots," Nat. Nanotechnol. 12(12), 1140–1147 (2017).
- ³⁴N. Taghipour, M. Dalmases, G. L. Whitworth, M. Dosil, A. Othonos, S. Christodoulou, S. M. Liga, and G. Konstantatos, "Colloidal quantum dot infrared lasers featuring sub-single-exciton threshold and very high gain," Adv. Mater. 35(1), 2207678 (2023).
- ³⁵C. Wang, B. L. Wehrenberg, C. Y. Woo, and P. Guyot-Sionnest, "Light emission and amplification in charged CdSe quantum dots," J. Phys. Chem. B **108**(26), 9027–9031 (2004).
- ³⁶J. Nanda, S. A. Ivanov, M. Achermann, I. Bezel, A. Piryatinski, and V. I. Klimov, "Light amplification in the single-exciton regime using exciton-exciton repulsion in type-II nanocrystal quantum dots," J. Phys. Chem. C 111(42), 15382–15390 (2007).
- ³⁷A. Kamath and P. Guyot-Sionnest, "The "energy gap law" for mid-infrared nanocrystals," J. Chem. Phys. 160(20), 200901 (2024).